# Surface-Based Remote Sensing of Marine Boundary-Layer Cloud Properties

ALLEN B. WHITE

*Cooperative Institute for Research in Environmental Sciences, University of Colorado/National Oceanic and Atmospheric Administration, Boulder, Colorado*

C. W. FAIRALL AND JACK B. SNIDER

*National Oceanic and Atmospheric Administration/Environmental Technology Laboratory, Boulder, Colorado*

(Manuscript received 3 June 1994, in final form 12 September 1994)

ABSTRACT

Surface-based measurements are used to define some of the important macrophysical and optical properties of marine clouds. These measurements were taken during five different marine field programs. A progression is made from a midlatitude marine stratocumulus regime with an average cloud fraction of 0.7 and a median cloud base of 460 m to a marine tropical regime with an average cloud fraction of 0.2 and a median cloud base of 1050 m. Measurements of the solar transmission coefficient taken during the Atlantic Stratocumulus Transition Experiment (ASTEX) were used in a radiative transfer algorithm to produce values of albedo, absorption, and optical depth. A microwave radiometer provided measurements of the liquid water path (LWP). For a given LWP, the ASTEX optical depths averaged a factor of 2 smaller than the optical depths observed during the marine stratocumulus phase of the First International Cloud Climatology Program Regional Experiment (FIRE) at San Nicolas Island, off the coast of southern California. The variability of boundary-layer aerosol concentrations measured during ASTEX is sufficient to produce a factor of 2 change in optical depth. Further evidence suggests that the cloud droplet effective radius was nearly a factor of 2 larger during ASTEX than during FIRE.

## 1. Introduction

Because oceans occupy roughly two-thirds of the earth's surface, marine clouds have a dominant effect on the global radiation balance. We know that marine clouds are dynamically, structurally, and microphysically distinct from continental clouds (Chertock et al. 1993). However, our current level of understanding is limited to the simplest case, marine stratocumulus. To better understand stratocumulus, as well as other marine cloud systems, we must continue not only to increase our observational database but also to take advantage of the improved treatment of cloud microphysics in models (e.g., Feingold et al. 1994).

Many observational methods have been used to study clouds including satellites, surface-based and airborne remote sensors, and in situ sensors mounted on aircraft, rawinsondes, tethersondes, and tetroons. While satellites provide the best approach to obtaining a global climatology of clouds on scales resolved by climate models, it is unlikely that all relevant cloud properties can be deduced from satellite-measured radiances alone (Fairall et al. 1990). Furthermore, to parameterize the effects of clouds correctly at the GCM scale, we need to understand the sub-grid-scale interactions of clouds and radiation. This problem requires a detailed set of observations, some of which can be provided by surface-based sensors.

In this paper, we examine several different types of marine boundary-layer (MBL) clouds using a combination of surface-based observations and radiative transfer theory. The observational data used in this analysis were obtained from five MBL field programs. Listed alphabetically, they are 1) the Atlantic Stratocumulus Transition Experiment (ASTEX), 2) the Coupled Ocean–Atmosphere Response Experiment (COARE), 3) the First ISCCP (International Satellite Cloud Climatology Program) Regional Experiment (FIRE) (marine stratocumulus phase), 4) the San Clemente Ocean Probing Experiment (SCOPE), and 5) the Tropical Instability Wave Experiment (TIWE).

The remainder of this paper is organized in the following way. Section 2 describes the instrumentation and measurements. The analysis of the measurements is divided into two parts. Section 3 presents cloud-base and cloud fraction statistics deduced from ceilometer data for four different marine climate regimes. Section 4 examines the ASTEX clouds in more detail. We calculate cloud optical properties using measurements of the solar transmission coefficient and a radiative transfer model. We investigate the relationship between optical depth and liquid water path (LWP), since this

*Corresponding author address:* Allen B. White, NOAA/ERL/ETL, R/E/ET7, 325 Broadway, Boulder, CO 80303.

relationship is often used to parameterize the effects of clouds in GCMs. The ASTEX results are compared with two other marine cloud studies. Section 5 presents a summary of our results.

## 2. Surface-based instrumentation and measurements

This section describes the instrumentation deployed during the five MBL field programs that have provided data for our analysis. The field programs are listed here in chronological order. For brevity, only those instruments and measurements pertaining to this work are discussed.

### *a. FIRE*

Ground-based measurements for the marine stratocumulus phase of FIRE were obtained on the northwest tip of San Nicolas Island (33°16′37″N, 119°34′34″W), which is located approximately 100 km southwest of Los Angeles, California. This site experiences marine flow most of the time. Extended time observations (ETO) were made on the island from March to October 1987. The instrumentation used during the ETO included an Eppley Model PSP pyranometer. The pyranometer has a standard Schott glass dome that is transparent in the 0.28-$\mu$m to 3-$\mu$m wavelength range. The sensor was sampled about once per second; half-hour mean and standard deviations of solar irradiance $R_s$ were stored. Further details are given by Fairall et al. (1990). In addition to the FIRE ETO, a period of intensive field operations (IFO) occurred from 29 June to 19 July 1987. A complete description of the FIRE IFO is given by Albrecht et al. (1988).

Scientists from the Colorado State University (CSU) operated a Vaisala CT 12K ceilometer at the ETO measurement site during the FIRE IFO. The CT 12K is commercially available and was originally designed for National Weather Service sites at airports. The system uses a GaAs diode laser to produce short (150 ns) high-intensity pulses of infrared radiation at 904-nm wavelength. The return signals from a large number of consecutive pulses are coherently summed to boost the signal-to-noise ratio. Each resulting 30-s profile of backscattered power at 15-m vertical resolution is analyzed to detect cloud layers using a specified cloud detection limit. In addition to measurements of cloud base, the ceilometer can also provide information on the overhead cloud fraction $f$ using a time series of the "cloud" or "no-cloud" status reported in the 30-s data. Additional details on operation of the CT 12K during the FIRE IFO are given by Schubert et al. (1987).

Also at the ETO site, scientists from the National Oceanic and Atmospheric Administration Environmental Technology Laboratory (NOAA/ETL) deployed their three-channel microwave radiometer (Hogg et al. 1983). The first channel operates at a wavelength of 1.46 cm (20.6 GHz), which is sensitive primarily to water vapor. The second channel operates at a wavelength of 0.95 cm (31.65 GHz), which is sensitive primarily to liquid water. The third channel operates at a wavelength of 0.33 cm (90.0 GHz), which is sensitive to both vapor and liquid. The three radiometers are coupled into a common antenna system with concentric beams of equal 2.5° width. A motor is used to steer the antenna system. However, the antenna beams were directed to zenith for the duration of the FIRE IFO. Atmospheric emission data from the 1.46-cm and 0.95-cm channels were used to retrieve integrated water vapor and LWP. The statistical retrieval technique is described in Hogg et al. (1983). The estimated uncertainty in the liquid measurement is 20% (Fairall et al. 1990). Radiometer data were averaged to 1-min resolution during the FIRE IFO.

### *b. TIWE*

The TIWE cruise on the R/V *Moana Wave* began on 18 November 1991 with a 7-day transit to the equator at 140°W, followed by 21 days on site and a 7-day return transit. Scientists from NOAA/ETL deployed five systems on the *Moana Wave* for this experiment: 1) an air–sea flux and bulk meteorological system, 2) a ship motion and navigation system, 3) a lidar ceilometer, 4) a 915-MHz radar, and 5) an Omega–Navaid-based rawinsonde system. As part of 1, the same pyranometer described in section 2a provided solar irradiance measurements. Hourly and 10-min averages were produced. The ceilometer used for TIWE was identical to the system described in section 2a. Ceilometer cloud-base information and lidar-reflectivity profiles were recorded at 30-s resolution.

The NOAA 915-MHz radar is a special seagoing version of the boundary-layer wind profiler developed at the NOAA Aeronomy Laboratory (Ecklund et al. 1988). At the heart of this compact design is a flat-plate, microstrip, phased-array antenna. A commercially available gyrostabilized platform is used to maintain the antenna level. Three independent beam orientations are produced by electronically changing the phasing. Winds are then obtained from the mean Doppler shifts of the three beams. Turbulence information can be deduced from the intensity and width of the Doppler spectra. The range-gated backscattered signals received by the radar can be converted into profiles of radar reflectivity or of the refractive index structure function $C_n^2$ (VanZandt et al. 1978). Two pulse resolutions were used to profile the lowest 5 km of the atmosphere. For most of TIWE a 105-m vertical resolution mode was used for the lowest 2 km, and a 420-m mode, sampled at every 210 m, was used to profile up to 5 km. For the last four days of the experiment, the 105-m mode was changed to a 60-m mode. The radar dwell time is a measure of how long the atmosphere is illuminated by any one particular radar beam.

For TIWE, the dwell time was approximately 26 s. Because three beams were operating at two pulse resolutions, there were six beams total. In part of the analysis that follows, we will be using data from the high-resolution vertical beam. Consecutive data from this beam are separated by roughly 5 min. The additional time was used by the radar control program to collect and process data from the other five beams, record accelerometer data from the gyrostabilized platform, and interrogate a Global Positioning Satellite receiver to log ship speed, course, and position.

Because a microwave radiometer was not available for the TIWE cruise, a new technique was developed for measuring LWP using ceilometer data in conjunction with vertical profiles of 915-MHz radar reflectivity (Chertock et al. 1993). Because 915-MHz radar reflectivity shows enhancement in clouds due to a combination of increased turbulence and scattering from large cloud droplets and/or precipitation, a reduction in reflectivity is expected near the boundary between a cloud and the free troposphere. When a cloud was present in the ceilometer beam, Chertock et al. (1993) examined the radar reflectivity profile for sharp reductions in $C_n^2$. A factor of 4 reduction in $C_n^2$ over 100 m was used as the criterion for determining cloud top. The LWP was then calculated assuming an adiabatic liquid water profile in the cloud (e.g., Albrecht et al. 1990).

Because it can be shown that in the absence of precipitation the enhancement in reflectivity in clouds for the relatively low-powered 32-cm wavelength radar is primarily due to turbulence, this technique is based on a $C_n^2$ definition of cloud top. Because of the unpredicted effects of entrainment and the intermittent characteristics of turbulence in general, the cloud top produced from this analysis may differ from the results obtained with an instrument that is more sensitive to cloud droplets. For thin clouds, a significant error arises from the 100-m range resolution of the radar. Also, for deep clouds or in cases of precipitation, the adiabatic assumption is likely to be invalid. Despite these shortcomings, the adiabatic values of LWP for the relatively thin (100–500 m) trade cumulus observed during TIWE agreed fairly well with LWP retrievals from the special sensor microwave/imager aboard the Defense Meteorological Satellite Program *F08* satellite (Chertock et al. 1993).

### c. *ASTEX*

#### 1) R/V *MALCOLM BALDRIGE*

The ASTEX cruise on the R/V *Malcolm Baldrige* began on 1 June 1992 with a 6-day transit to the eastern Atlantic, followed by 22 days on site. The cruise operations are summarized by Bluth and Albrecht (1993). The on-site hourly positions in the experimental region are given in Fig. 1. In addition to the systems listed in section 2b, a NOAA/ETL dual-channel microwave radiometer was deployed on the *Malcolm Baldrige* during ASTEX. The radiometric system is similar to that described in section 2a, except that it operates at 20.6 and 31.65 GHz. Radiometric data were stored at a 30-s data rate. The 915-MHz radar was operated with 60-m and 420-m pulse resolutions.

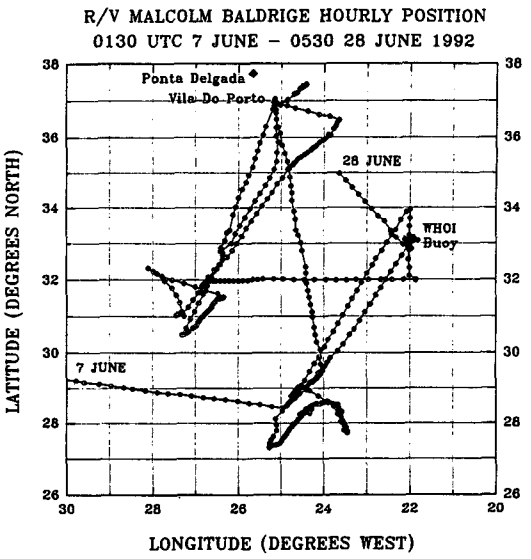


FIG. 1. Hourly positions of the R/V *Malcolm Baldrige* during ASTEX (from Bluth and Albrecht 1993).

Conducted in conjunction with ASTEX was the Marine Aerosol and Gas Exchange Experiment. Scientists from the NOAA Atlantic Oceanographic and Meteorological Laboratory (AOML) deployed a TSI Inc. Model 3010 Condensation Particle Counter to measure condensation nuclei (CN) concentration onboard the *Malcolm Baldrige*. The instrument is sensitive to 50% of 0.01-$\mu$m particles and has a maximum detectable particle size greater than 8 $\mu$m. The particle concentration range is 0.0001–10 000 per cm$^3$. The CN data were stored as 1-min averages and later averaged to 10-min resolution.

#### 2) PORTO SANTO ISLAND

Another of the ASTEX measurement platforms was situated on Porto Santo Island in the Madeira Archipelago (Portugal). The site was located at the northern (windward) tip of the island (33°5′2″N, 16°20′49″W). Island operations are summarized by Bluth and Albrecht (1993). Data from the following NOAA/ETL instruments are employed in this paper: a three-channel microwave radiometer, an Eppley Model PSP pyranometer, and an 8-mm (35 GHz) Doppler radar. Scientists from CSU also operated remote sensors, including a Vaisala laser ceilometer. The radiometer, pyranometer, and ceilometer were previously described in section 2a. The NOAA/ETL 8-mm ($K_a$ band) Dopp-

ler radar was originally discussed by Pasqualucci et al. (1983). Since then, the radar has undergone design changes to improve its range resolution and sensitivity. Currently, the radar operates with a 0.5° beamwidth and a 37-m pulse width. The sensitivity is defined in terms of the radar reflectivity factor in decibels, dBZ. The radar will detect a −50 dBZ echo at 1-km range and a −31 dBZ echo at 10-km range (Kropfli et al. 1995). Because of the enhanced sensitivity and vertical resolution, this radar is ideally suited to boundary-layer cloud studies.

### d. COARE

The R/V *Moana Wave* departed Hawaii on 27 October 1992 with an 11-day transit to Pohnpei, Micronesia. The four-month experiment was broken up into three separate cruise legs. The first leg began 9 November with a 2-day transit to the COARE operations area (COA), followed by 23 days on site and a 5-day transit to Guam. The second leg began 13 December with a 6-day transit to the COA, followed by 22 days on site and a 5-day return transit to Guam. The third and final leg began 23 January 1993 with a 5-day transit to the COA, followed by 17 days on site and a 3-day return transit to Guam. For the first two legs, the *Moana Wave* was positioned in the COARE Intensive Flux Array near 2°S, 156°E. For the third leg, the *Moana Wave* stayed at this location for 8 days and then was moved to the equator for 9 days, before returning to Guam. The shipboard instrumentation deployed during COARE was the same as that described in section 2c.

### e. SCOPE

The SCOPE cruise on the R/V *Titan* began on 14 September 1993 and ended on 26 September 1993. The cruise took place between San Clemente and Santa Catalina Islands, off the coast of southern California. The shipboard instrumentation was similar to that described in section 2c. In our analysis, ceilometer data from SCOPE and FIRE were combined because of the close proximity of the experiment locations and to better match the volume of data observed in the other field programs.

## 3. Macrophysical cloud properties

In this section, we use the ceilometer data to examine the bulk properties of boundary-layer clouds observed in four different marine climate regimes. Due to the limited length of record for each of the datasets we used, one should not view these analyses as being climatologically definitive. However, because these data come from marine regimes with modest seasonal variability and the seasons we sampled are characterized by weak synoptic activity, we propose that each of the extended time series is sufficient to estimate a seasonal cloud climatology for the analyzed region.

### a. Interpretations and limitations of ceilometer data

When viewing the ceilometer-deduced cloud properties, the reader should be aware of several key points. First, because the maximum vertical range of the ceilometer is 3480 m, cirrus and other mid- to high-level clouds cannot be detected. Second, the lidar beam points vertically. Therefore, depending on the horizontal distribution of clouds, the overhead time-averaged cloud fraction deduced from the ceilometer may not be consistent with the true area-averaged cloud fraction obtained from satellite measurements. Third, the cloud base determined by the ceilometer may differ from the base that is visible to the eye or that may be measured by different instruments such as millimeter wavelength radars (Uttal and Intrieri 1993). Fourth, for a cloud that tilts in the presence of wind shear, the ceilometer will actually report the height of the side of the cloud as it passes over the instrument. Finally, there are instances when the ceilometer determines the sky condition to be totally obscured, but no cloud base can be detected. These situations occur at low and middle latitudes in fog or precipitation; cases we feel should naturally be included in a computation of cloud fraction. In other instances, the ceilometer reports partially obscured conditions, usually representing a very thin cloud that attenuates the beam but does not produce a clearly defined "hard return" that can be identified as a cloud base. These data were discarded prior to our analysis.

### b. Cloud fraction and cloud base

The ceilometer data are presented in two formats. Summary statistics, along with the names, dates, locations, and cloud types observed for each of the field programs, are given in Table 1. The experiments are organized in the order shown to provide a logical transition from the midlatitude stratocumulus-topped MBL to the tropical convective MBL. Diurnally averaged cloud fraction and cloud base, as well as cloud-base frequency distributions, are shown graphically in Fig. 2. The curves for ASTEX are derived from the ship-based ceilometer measurements.

### c. Discussion

The cloud-fraction and cloud-base statistics exhibit both expected and unexpected behavior. For example, the diurnally averaged cloud fraction curves shown in Fig. 2 for FIRE/SCOPE and ASTEX show marked similarities during the daytime but differ for at least part of the night. The decrease in cloud fraction from midmorning to early afternoon observed for these two cases is consistent with the theory of boundary-layer decoupling reviewed by Driedonks and Duynkerke (1989). For both of these cases, the minimum cloud

TABLE 1. Cloud statistics generated from extended time series of ceilometer data.

| Experiment name | Dates | Location Latitude Longitude | Total number of 30-s profiles | Cloud fraction | Cloud base (m) 20th percentile | Cloud base (m) 50th percentile | Cloud base (m) 80th percentile | Primary cloud types |
|---|---|---|---|---|---|---|---|---|
| FIRE | July 1987 | San Nicolas Island<br>Eastern Pacific<br>33°N<br>120°W | $8.05 \times 10^4$ | 0.69 | 300 | 457 | 750 | Marine stratus |
| SCOPE | September 1993 | R/V *Titan*<br>Eastern Pacific<br>33°N<br>118°W | | | | | | |
| TIWE | November–December 1991 | R/V *Moana Wave*<br>Equatorial Pacific<br>0<br>140°W | $5.68 \times 10^4$ | 0.26 | 625 | 945 | 1585 | Trade cumulus |
| ASTEX | June 1992 | R/V *Malcolm Baldrige*<br>Eastern Atlantic<br>27–37°N<br>22–27°W | $5.81 \times 10^4$ | 0.45 | 594 | 1021 | 1463 | Marine stratus<br>Trade cumulus |
| | | Porto Santo Island<br>33°N<br>16°W | $3.07 \times 10^4$ (1-min profiles) | 0.56 | 556 | 938 | 1494 | Marine stratus<br>Trade cumulus |
| COARE | November 1992–February 1993 | R/V *Moana Wave*<br>Western Pacific<br>2°S–5°N<br>153°–157°E | $1.26 \times 10^5$ | 0.22 | 686 | 1052 | 1844 | Trade cumulus (suppressed)<br>Cumulonimbus (convective) |

fraction in the diurnal cycle occurs at 1430 LST. The increase in cloud fraction that follows may be caused by reconnection of the cloud layer with the subcloud layer. It is interesting to note that the FIRE/SCOPE cloud fraction remains high overnight, while the ASTEX cloud fraction shows considerably more variability. It is also somewhat surprising to find that although deep convection and rainfall were observed much more frequently during COARE than during TIWE, the average boundary-layer cloud fraction for TIWE is slightly higher than for COARE (see Table 1). Note, however, the limited vertical range of the ceilometer. Neither of the two tropical cases shows any significant diurnal variation in cloud fraction, which helps to demonstrate how differently the tropical and midlatitude marine boundary layers react to solar radiation.

The only site with a significant diurnal variation in cloud base is COARE. The peaks near 0330 and 1730 LST may indicate periods that were slightly more favored for deep convection. The large difference between the average bases observed during FIRE/SCOPE and ASTEX is due to a combination of associated factors, including distance from the coastline, sea surface temperature, and average strength of subsidence above the MBL. The FIRE/SCOPE region is in the classic strong subsidence area in the southeast corner of a high pressure zone, whereas the ASTEX region is closer on average to the center of the high where weaker subsidence leads to the cloud transition being studied in that experiment.

The most descriptive of the ceilometer-deduced statistics are the cloud-base frequency distributions (Fig. 2). The FIRE/SCOPE distribution is made up almost completely of stratocumulus and thus, as expected, has the narrowest width and the lowest median value of all the distributions. The TIWE and COARE distributions are composed of two distinct parts. The lower part of both distributions has a well-defined peak between 500 and 900 m that corresponds to trade cumulus forming near the lifting condensation level. Keeping in mind that the ceilometer also sees the heights of the sides of thick clouds, the tail of these distributions (i.e., the part from 1 to 4 km) indicates deeper convection. The ASTEX distribution is unlike the other three cases. The region from 500 to 1500 m is made up of stratus, trade cumulus, and the so-called scud clouds that form in the decoupled boundary layer.

To help illustrate the diverse nature of the ASTEX clouds, we examine the cloud structure observed on the *Malcolm Baldrige* for two of the experiment days. Hourly time series of cloud fraction, cloud base, cloud top, and LWP are shown for 16 June (Fig. 3) and 21 June (Fig. 4). On 16 June, the average cloud fraction was 0.89 with a median cloud base of 650 m. On 21 June, the average cloud fraction was 0.85, but the median cloud base was 1500 m. In Fig. 3, we see varia-

tions in cloud depth that correlate well with the observed LWP. Drizzle was observed at the surface between 0408 and 0410 UTC. In Fig. 4, the stratus layer is higher and thinner than in Fig. 3. The three sharp downward excursions in cloud base reflect scud clouds forming in the boundary layer. The first two excursions are accompanied by little change in the LWP. Therefore, it is unlikely that these clouds extend up to the height of the trade inversion, as indicated by our simple radar algorithm. However, there is a sharp increase in LWP for the third case. The 30-s cloud-base data for this period show a mushrooming effect indicating a deeper cloud.

## 4. Cloud optical properties

In this section, we examine the optical properties of clouds using measurements of $R_s$ and LWP described in section 2 and a plane-parallel radiative transfer model. The results we obtain for ASTEX are compared to the results from TIWE (Chertock et al. 1993) and FIRE (Fairall et al. 1990).

### *a. Transmission coefficient*

We used the measurements of $R_s$ to infer the transmission coefficient Tr. First we used observations of $R_s$ during cloud-free periods to estimate a clear-sky solar diurnal cycle. Then Tr was computed as the ratio of $R_s$ to our estimate of the average clear-sky value taken from the solar curve. Given the latitude, longitude, Julian date, and time of day, we also calculated the solar zenith angle $\theta$.

### *b. Cloud fraction and zenith angle corrections*

Although several instances of solid cloud (i.e., $f = 1.0$) were observed during FIRE, the bulk of the data for ASTEX and TIWE is for broken clouds (see Table 1). To complicate matters further, the values of $f$ and LWP were measured using upward-looking narrow-field-of-view instruments (i.e., the ceilometer and radiometer), whereas the values of Tr were based on pyranometer measurements that are hemispheric.

For the broken cloud case Chertock et al. (1993) developed a set of equations (their model 3) that take into account cloud fraction and the zenith-angle dependence of cloud fraction $f(\theta)$. Following their notation, the equation for the effective plane-parallel transmission coefficient $T_{pp}$ is given by

$$T_{pp} = \frac{\mathrm{Tr} - [1 - f(\theta)]}{f(\theta)}. \quad (1)$$

This formulation is based on a simple linear partitioning of clear and cloudy regions. The empirical relation used to correct $f$ for zenith angle dependence is taken from Feigelson (1984):

$$f(\theta) = 1 - (1 - f)\exp\{-bf[\sec(\theta) - 1]\}. \quad (2)$$

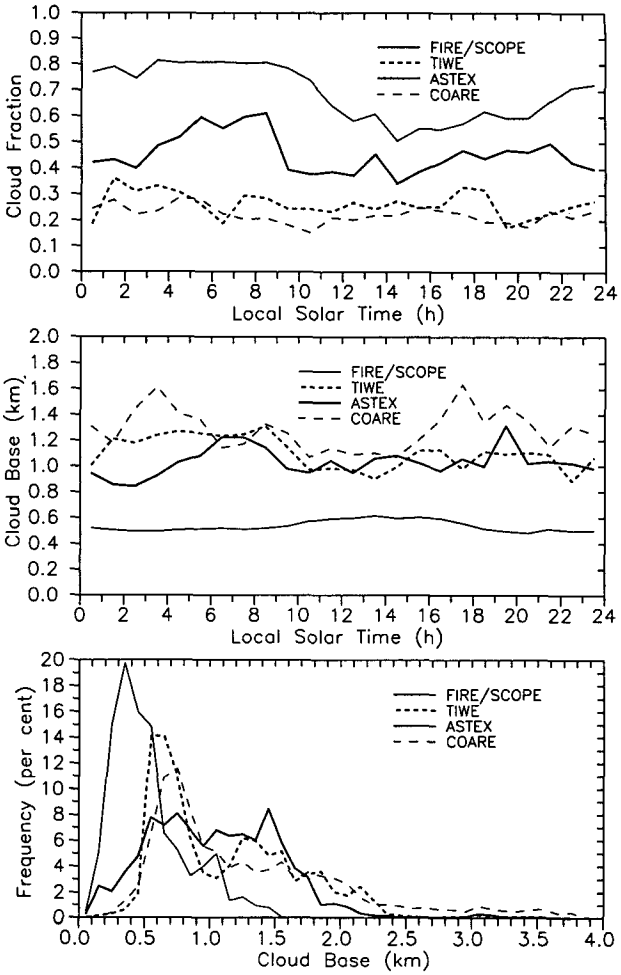


FIG. 2. Diurnally averaged cloud fraction (top panel), cloud base (middle panel), and cloud-base frequency distribution (bottom panel) calculated from extended time series of ceilometer data. The ASTEX data shown are from the ship-based ceilometer.

For marine conditions, $b = 1$. Note that if the ceilometer measures $f = 1$, then $f(\theta) = 1$ for all values of $\theta$ and $T_{pp} = \mathrm{Tr}$.

### *c. Albedo and optical depth*

We used the plane-parallel radiative transfer algorithm of Stephens (1978), as revised by Stephens et al. (1984), to obtain values of albedo, Re, and optical depth $\tau$. The Stephens parameterization is based on the two-stream, two-band approximation of Coakley and Chylek (1975). This model was originally intended to provide estimates of Tr, Re, and absorption Ab in terms of $\tau$ and $\theta$. However, we invert the algorithm to provide Re, Ab, and $\tau$ in terms of Tr and $\theta$. This approach was first used by Fairall et al. (1990) for the FIRE ETO dataset and again by Chertock et al. (1993) for the TIWE dataset. The Stephens parameterization has been fit to measurements from a variety of real clouds and

is expected to be applicable to some 15 cloud types. A look-up table of values for single-scattering albedo and backscatter fraction is given as a function of $\tau$ and $\mu = \cos\theta$. These values are based on results of sophisticated 10-layer, 15-band radiative transfer computations. The revised look-up table (Stephens et al. 1984) is used in our analysis. We used a value of 0.05 for the ocean albedo.

The results we obtain from inserting Tr and $\theta$ into the Stephens algorithm are representative of both clear and cloudy regions. Therefore, the model output Re and $\tau$ are in effect sky averaged or system optical properties. On the other hand, if we wish to differentiate the effects of the broken clouds by treating them in a plane-parallel manner, then we must use $T_{pp}$ instead of Tr as model input. The results we obtain will then pertain only to the cloudy part of the sky. We will refer to these optical properties as the plane-parallel albedo $R_{pp}$ and the cloud optical depth $\tau_c$.

### d. Diurnal and campaign statistics

Figure 5 shows the 22-day diurnally averaged optical properties computed from the ASTEX 10-min data. Angle brackets are used to denote diurnal averages. The solid curves are computed directly from the shipboard measurements of $f$, Tr, $\theta$, and the Stephens algorithm. The dashed curves are computed from the shipboard measurements modified by (1) and (2). We inserted each 10-min value of $T_{pp}$ and $\theta$ into the Stephens algorithm to produce individual time series of $R_{pp}$ and $\tau_c$ before computing the diurnal average.

The diurnal variations of cloud properties in ASTEX are quite different from the equatorial Pacific region studied in TIWE (Chertock et al. 1993). In TIWE, diurnal variations of cloud optical depth and cloud fraction were negligible, so variations in system albedo and transmission coefficient were dominated by solar zenith angle effects. In ASTEX, the cloud fraction had a substantial diurnal variation with a maximum of about 0.55 at sunrise and a minimum of 0.28 well after sunset. As shown in Fig. 5, this leads to a steady decrease of $\langle\tau\rangle$ during the daytime and a skewing of the albedo and transmission coefficient curves.

In addition to diurnal cycles, campaign mean/median values were computed. The results for ASTEX and TIWE are summarized in Table 2. Ship-based measurements of relevant surface meteorological quantities are given in addition to the cloud properties. The effect of the diurnal cycle on the shortwave energy budget is reflected in the disparity between the median and average values and the large standard deviations observed for solar irradiance and total surface energy.

The clouds in ASTEX had slightly lower cloud bases (870 m for ASTEX versus 890 m for TIWE) and were slightly thinner (250 m versus 310 m) but had substantially lower LWP (120 g m$^{-2}$ versus 210 g m$^{-2}$) and optical depths (10 versus 18). However, when combined with a greater average cloud fraction (0.38 versus 0.26), the ASTEX clouds actually lead to a greater total system albedo (0.27 versus 0.22). The solar irradiance was larger for ASTEX despite a larger system albedo, because the experiment was conducted proximate to the Northern Hemisphere summer solstice.

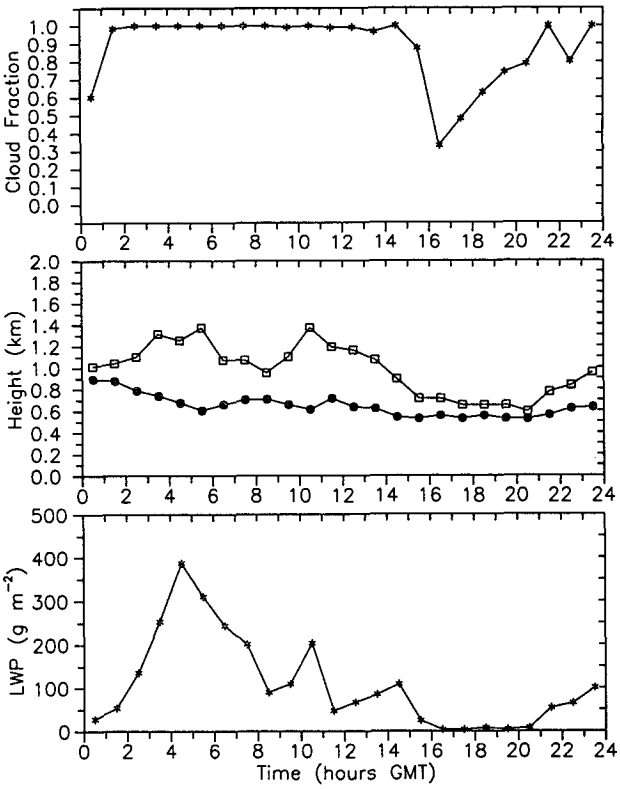


FIG. 3. Hourly time series of cloud data observed from the ship on 16 June. The top panel shows the overhead cloud fraction, the middle panel shows cloud base (solid circles) and cloud top (squares), and the bottom panel shows LWP.

### e. The $\tau$ versus LWP relationship

As mentioned earlier, one of our goals was to investigate the $\tau$ versus LWP relationship, because it is often used to parameterize the radiative effects of clouds in large-scale models. For example, Stephens (1978) has shown that

$$\tau = (3/2)\,\mathrm{LWP}/(\rho_w r_e), \qquad (3)$$

where the effective radius $r_e$ is defined as the ratio of the third moment to the second moment of the cloud droplet distribution and $\rho_w$ is the water density. Alternatively, Fairall et al. (1990) have shown that for a lognormal droplet size distribution and a linear profile of liquid water

$$\tau = (3/5)2^{5/6}(3/4\pi\rho_w)^{2/3} \times \exp(-\sigma_x^2)\Gamma^{-1/6}N^{1/3}\mathrm{LWP}^{5/6}, \qquad (4)$$

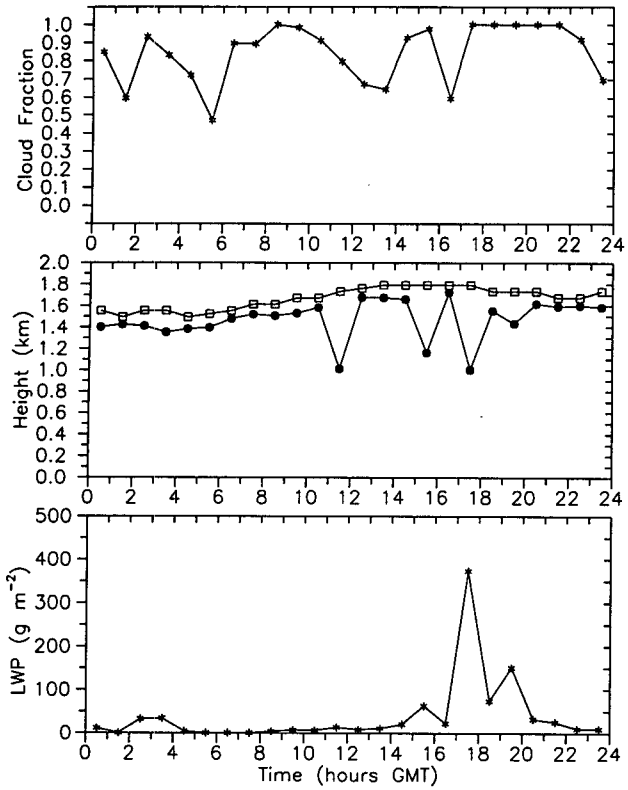


FIG. 4. Same as Fig. 3 except for 21 June.

where the coefficient $\Gamma$ is approximately 0.0002 times the mixed-layer total water concentration (see Albrecht et al. 1990), $\sigma_x$ is the distribution width, and $N$ is the cloud droplet number concentration (assumed to be independent of height in the cloud).

We used the diurnal statistics $\langle \tau_c \rangle$, $\langle \text{LWP} \rangle$, and $\langle f \rangle$ to investigate the relationship between optical depth and liquid water. Because the radiometer points vertically and sees essentially the same distribution of clear sky and clouds that the ceilometer sees, we use $\langle \text{LWP} \rangle / \langle f \rangle$ to define the cloud LWP. The island- and ship-based results for ASTEX are shown in Fig. 6, along with the results obtained from TIWE and FIRE. The FIRE relationship was obtained from essentially plane-parallel clouds (i.e., $f \approx 1.0$), so we expect ASTEX and TIWE data points to lie near the solid line. The lower bounds used for the plot are consistent with the approximate lower limits on the accuracy of our values for $\tau$ and LWP.

### *f. Discussion*

The scatter evident in Fig. 6 may be attributable to a number of factors. First and foremost is our assumption that we may treat broken clouds in a plane-parallel manner. When working with broken clouds in the manner described above, there is no way to avoid situations where the sun is behind a cloud that is not directly above the radiometer, and vice versa. This idea is supported by Fig. 6, where the data derived from measurements collected near solar noon show significantly less scatter than the general population of points. Another example is given in Fig. 7, where 10-min data for the nearly solid cloud fraction day observed on 16 June (see Fig. 3) show less scatter, except for small values of $\tau_c$ and LWP. Second, the correction for the zenith angle dependence of cloud fraction given by (2) can produce significant errors at large zenith angles (see Fig. 5). These errors will carry through to the estimates of $T_{pp}$ derived from (1). Third, the simple linear partitioning of clear and cloudy regions given by (1) has the tendency to produce erroneous results for cloud fractions less than about 0.1. Finally, there is evidence suggesting that diurnal averages may not be appropriate. For example, the measurements of boundary-layer aerosol concentration taken onboard the *Malcolm Baldrige* during ASTEX, shown in Fig. 8, identify variability that cannot be characterized as diurnal.

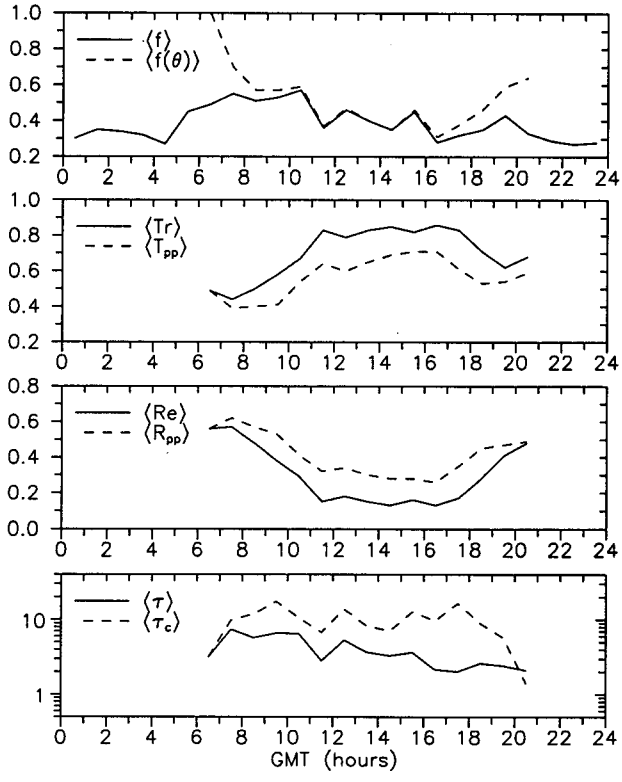


FIG. 5. Diurnally averaged optical properties observed during ASTEX. Starting at the top, two curves are given for each of the following: cloud fraction, transmission coefficient, albedo, and optical depth. The solid curves are based on cloud fraction measured at zenith and include the effects of clear sky and clouds. The dashed curves take into account zenith angle variation and differentiate the effects of clouds. Cloud fraction and solar transmission data were obtained onboard the R/V *Malcolm Baldrige*.

TABLE 2. Campaign hourly data statistics.

| Variable | ASTEX | | | TIWE |
|---|---|---|---|---|
| | Median | Average | Sigma | Average |
| Ship speed (m $s^{-1}$) | 6.0 | 4.8 | 2.58 | 0.7 |
| 10-m wind speed (m $s^{-1}$) | 4.7 | 4.4 | 1.79 | 6.4 |
| 10-m wind direction (°) | 33 | 34 | 77 | 108 |
| Sea surface temperature (°C) | 20.7 | 20.7 | 1.05 | 27.2 |
| 14-m air temperature (°C) | 20.0 | 19.8 | 1.10 | 26.9 |
| Surface saturation humidity (g $kg^{-1}$) | 15.2 | 15.2 | 0.97 | 22.5 |
| 14-m humidity (g $kg^{-1}$) | 10.5 | 10.5 | 1.35 | 17.1 |
| 14-m relative humidity (%) | 73.2 | 72.8 | 7.71 | 77.3 |
| Sensible heat flux (W $m^{-2}$) | 8 | 8 | 5.75 | 4 |
| Latent heat flux (W $m^{-2}$) | 75 | 76 | 32.2 | 101 |
| Surface stress (N $m^{-2}$) | 0.023 | 0.029 | 0.020 | 0.054 |
| Surface solar irradiance $R_s$ (W $m^{-2}$) | 58 | 255 | 320 | 232 |
| Surface longwave irradiance (W $m^{-2}$) | 346 | 350 | 21.8 | 401 |
| Total surface energy (W $m^{-2}$) | −98 | 83 | 305 | 52 |
| Transmission coefficient Tr | 0.73 | 0.72 | 0.21 | 0.74 |
| Albedo Re | 0.26 | 0.27 | 0.20 | 0.22 |
| Cloud optical depth $\tau_c$ | 4.9 | 10.1 | 21.9 | 17.7 |
| Cloud fraction at zenith $f$ | 0.26 | 0.38 | 0.37 | 0.26 |
| Cloud base (m) | 869 | 1007 | 515 | 886 |
| Cloud thickness (m) | 220 | 251 | 163 | 313 |
| Cloud liquid water path[1] LWP (g $m^{-2}$) | | 123 | | 209 |

[1] For ASTEX, the average cloud LWP is defined as the average LWP measured by the radiometer divided by the average cloud fraction measured at zenith.

If we consider only the ASTEX and TIWE points in Fig. 6 that were derived from measurements taken near solar noon, we then can place a line through these points that lies roughly a factor of 2 beneath the FIRE relationship. The study by Albrecht et al. (1990) showed that the marine stratocumulus clouds observed during FIRE contained nearly adiabatic profiles of liquid water. If we assume the same $r_e$ or $N$ can be used to characterize the clouds during FIRE, ASTEX, and TIWE, then the near-solar-noon data in Fig. 6 would suggest that the ASTEX and TIWE clouds are superadiabatic in water content. A more plausible explanation would be that $r_e$ and/or $N$ were different for ASTEX and TIWE. For example, FIRE took place much closer to a densely populated coastline than ASTEX, while TIWE occurred in a pristine marine environment, far away from any continental landmass. Because continental aerosols are generally smaller than maritime aerosols, we might expect FIRE to have a higher mean concentration of the smaller aerosols, which would lead to a smaller mean $r_e$ and a larger optical depth for a given LWP. Satellite observations do indicate higher cloud albedo near the California coast (Minnis et al. 1992), consistent with greater concentration of cloud condensation nuclei (CCN) associated with continental aerosol sources.

We can use the boundary-layer aerosol data shown in Fig. 8 to investigate the impact of aerosols on optical depth for the ASTEX clouds. Here, we must make the assumption that the particle concentration measured at the surface is directly proportional to the number of activated CCN. Among other reasons, this assumption may not be valid when the cloud layer is decoupled from the surface for an extended period. Furthermore, the recent work of Anderson et al. (1994) has shown poor correlation ($r = 0.33$) between ambient aerosol concentration and the number of cloud droplets determined by a counterflow virtual impactor. Because aerosol measurements were taken only during certain observing periods, we will use the 10-min $\tau_c$ and LWP data to increase the size of our dataset. We excluded data taken while precipitation was observed at the surface.

Figure 9 shows the 10-min ASTEX data plotted for two ranges of aerosol concentration. Although there is a significant amount of scatter, most of the ASTEX data with "low" aerosol concentrations (i.e., less than 200 $cm^{-3}$) lie below the FIRE line, while much of the ASTEX data with "high" aerosol concentrations (i.e., greater than 800 $cm^{-3}$) lie above the FIRE line. The FIRE relationship can be written as

$$\log_{10}(\tau) = m_F \log_{10}(\mathrm{LWP}) + y_F, \qquad (5)$$

where $m_F$ and $y_F$ are the slope and $y$ intercept that fit the FIRE IFO dataset (Fairall et al. 1990). Each of the ASTEX data points in Fig. 9 can also be characterized by a slope $m_A$ and a $y$-intercept $y_A$. Since the near-noon data in Fig. 6 suggest that the FIRE, ASTEX, and TIWE datasets can all be described by roughly the same slope, then we will let $m_A = m_F = 0.88$. Now we can find a $y_A$ value for each of the points in Fig. 9. The

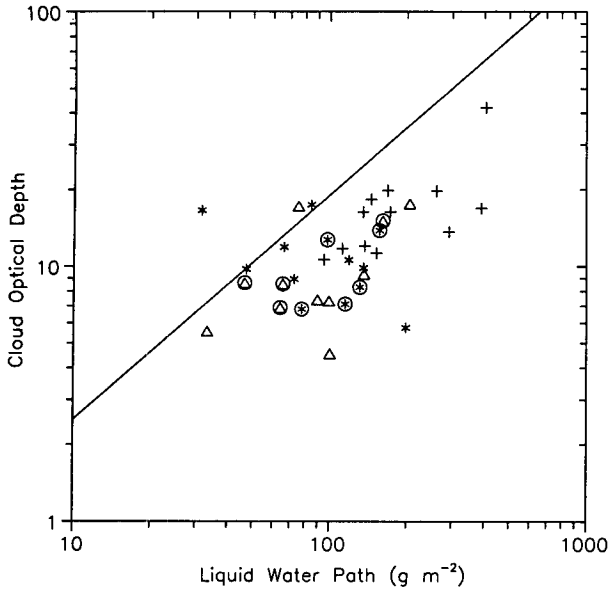


FIG. 6. Cloud optical depth vs LWP. The symbols plot diurnal averages derived from ASTEX ship data (asterisks), ASTEX island data (triangles), and TIWE data (pluses) (Chertock et al. 1993). The line shows the relationship for FIRE (Fairall et al. 1990). The circles classify data derived from measurements taken near solar noon ($\theta \leq 15°$).

antilog of the ratio $(y_A/y_F)$ gives the linear ratio between the optical depths. The low aerosol concentration data have an average concentration of 131 cm$^{-3}$ and on average lie a factor of 0.7 below the FIRE line. The high aerosol concentration data have an average concentration of 1128 cm$^{-3}$ and on average lie a factor of 1.4 above the FIRE line. If we assume that $\tau \propto N^{1/3}$, as in (4), then the average ratio of aerosol concentrations would change the optical depth by a factor of $(1128/131)^{1/3} = 2.0$. This value agrees with the observed change in optical depth (i.e., $1.4/0.7 = 2.0$).

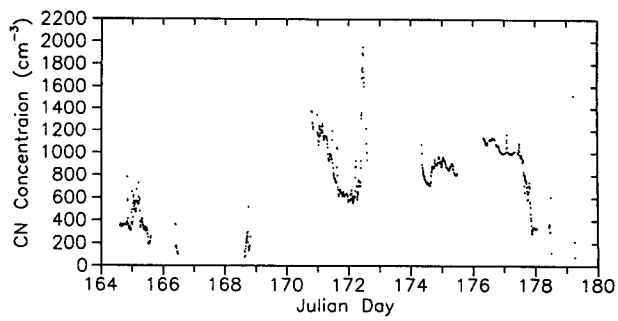


FIG. 8. The 10-min averages of condensation nuclei concentration measured onboard the R/V *Malcolm Baldrige* during ASTEX.

There is also independent evidence suggesting that the mean effective radius observed during the FIRE IFO was less than that observed during ASTEX. Han et al. (1995) have computed cloud droplet sizes for the FIRE ETO and FIRE IFO periods using the Advanced Very High Resolution Radiometer observations of the (ISSCP) data analysis (Rossow and Schiffer 1991). Their results show $r_e = 8$ $\mu$m for the FIRE IFO period. This is an estimate of the effective radius near cloud top (Han et al. 1995). Frisch et al. (1995) show that profiles of modal radius $r_m$ can be retrieved from ver-

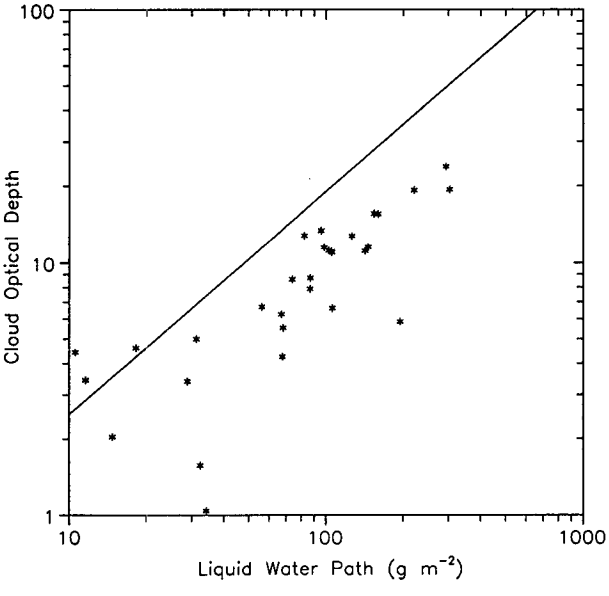


FIG. 7. Cloud optical depth vs LWP. The symbols plot 10-min averages derived from ASTEX ship data for 16 June. The line is for the FIRE relationship.

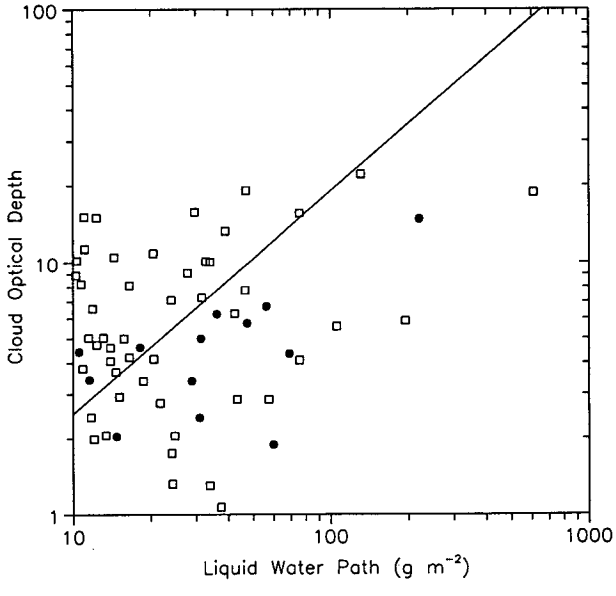


FIG. 9. Cloud optical depth vs LWP. The ASTEX 10-min ship-based data are plotted for instances of condensation nuclei concentration greater than 800 cm$^{-3}$ (squares) and less than 200 cm$^{-3}$ (solid circles). The line is for the FIRE relationship.

tical profiles of radar reflectivity and microwave radiometer measurements of the LWP by assuming a cloud droplet distribution shape and characteristic width $\sigma_x$. Assuming a lognormal distribution with $\sigma_x = 0.35$ $\mu$m, they retrieved $r_m = 8-12$ $\mu$m near cloud top during ASTEX using data from the 8-mm radar described in section 2c. By taking the ratio of the third moment to the second moment of the assumed lognormal distribution, it can be shown that $r_e = 1.36r_m$. The observed values of $r_m$ then translate into values of $r_e$ ranging from 11 to 16 $\mu$m for the ASTEX clouds, which from (3) is consistent with the factor of 2 difference in FIRE and ASTEX optical depths.

## 5. Summary and conclusions

We have given an analysis of marine boundary-layer cloud structure using a suite of surface-based sensors and a plane-parallel radiative transfer algorithm. The cloud fraction and cloud-base statistics calculated from ceilometer data give us a description of the large-scale properties of MBL clouds. A simple model using a plane-parallel radiative transfer algorithm gives us some of the important bulk optical properties of the clouds.

The FIRE and ASTEX diurnally averaged cloud fractions shown in Fig. 4 indicate boundary-layer decoupling beginning before 1200 LST and leading to a minimum in cloud fraction at approximately 1430 LST. This feature was directly observed during FIRE by Hignett (1991). The trade cumulus observed during TIWE were in effect always decoupled. Vertical profiles of radar reflectivity consistently indicated a substantial cloud-base inversion. The tropical cloud-base distributions are identified by a narrow peak corresponding to trade cumulus forming at the lifting condensation level and long tails characterizing deeper convection or the sides of tilted clouds. The FIRE/SCOPE cloud-base distribution is made up almost entirely of marine stratocumulus in the lowest 1 km. Because ASTEX encompassed both stratocumulus and trade cumulus regimes, a complex distribution of cloud bases was observed for that experiment.

Using optical cloud properties deduced from surface-based measurements of the transmission coefficient and a radiative transfer model, we investigated the relationship between optical depth and liquid water for ASTEX and compared our result with the results obtained for FIRE and TIWE. Our comparison, shown in Fig. 6, indicated that the TIWE and ASTEX clouds formed in significantly cleaner air masses on average than the FIRE clouds. This result was investigated further by taking advantage of the shipboard aerosol measurements recorded during ASTEX (see Fig. 8). We found a factor of 2 change in the $\tau$ versus LWP relationship associated with a factor of 8 variation in aerosol concentration observed just within the ASTEX dataset, a direct demonstration of the so-called Twomey effect (Twomey 1977). Independent droplet size information deduced from 8-mm radar and satellite observations also suggest that the ASTEX cloud droplets were on average a factor of 2 larger than the FIRE cloud droplets.

These results underscore the need to make detailed long-term measurements of cloud microphysical properties at different locations around the earth. Because of the constraints involved with a shipboard deployment, the method described in this paper is certainly not the best way to accomplish this undertaking. In an attempt to obtain meaningful ensemble averages of cloud properties, it was necessary for us to use long-term (diurnal) averaging to compensate for our sampling inadequacies. One way to avoid the averaging requirement would be to take whole-sky measurements. Recent advancements in whole-sky imaging technology are currently being used in the Department of Energy Atmospheric Radiation Measurement (ARM) Program.

The observed similarities between the cloud statistics generated from ship data and island data for the ASTEX period (see Table 1 and Fig. 6) suggest that for some maritime regimes, climatologically representative cloud statistics may be obtained from a properly placed island measurement site. Because of the prohibitive cost of extended ship operations and the limited space offered by smaller semipermanent seagoing platforms, such as buoys, this result is important to anyone interested in obtaining extremely long time series. Of course, the ASTEX result may not be valid for a more convective maritime regime, where land/sea differences in latent and sensible heating may affect the amount and types of clouds and precipitation patterns that are observed. Furthermore, the FIRE result cautions us that cloud microphysical measurements obtained from an island situated too close to a much larger land mass will not be representative of the undisturbed marine aerosol number concentration and size distribution. Although aerosol measurements were not taken on Porto Santo Island, it is clear from Fig. 8 that even the R/V *Malcolm Baldrige* was close enough to the mainland for the ship-based aerosol measurements to be influenced, under certain meteorological conditions, by continental aerosol sources.

*Acknowledgments.* The authors wish to express special thanks to Paul Ciesielski and Wayne Schubert of Colorado State University for providing FIRE and ASTEX ceilometer data; Alex Pszenny, formerly of NOAA/AOML, for providing ASTEX aerosol measurements; and Shelby Frisch of NOAA/ETL for sharing ASTEX cloud radar results. This work was supported by the NOAA Climate and Global Change Program, the Office of Naval Research, and the Department of Energy ARM Program.

## REFERENCES


Albrecht, B. A., D. A. Randall, and S. Nicholls, 1988: Observations of marine stratocumulus clouds during FIRE. *Bull. Amer. Meteor. Soc.*, **69,** 618–626.

——, C. W. Fairall, D. W. Thomson, A. B. White, J. B. Snider, and W. H. Schubert, 1990: Surface-based remote sensing of the observed and the adiabatic liquid water content of stratocumulus clouds. *Geophys. Res. Lett.*, **17,** 89–92.

Anderson, T. L., D. S. Covert, and R. J. Charlson, 1994: Cloud droplet number studies with a counterflow virtual impactor. *J. Geophys. Res.*, **99,** 8249–8256.

Bluth, R. T., and B. A. Albrecht, 1993: Atlantic Stratocumulus Transition Experiment and Marine Aerosol and Gas Exchange experiment summary: Part II—Platform operations. Dept. of Meteorology, The Pennsylvania State University, 277 pp.

Chertock, B., C. W. Fairall, and A. B. White, 1993: Surface-based measurements and satellite retrievals of broken cloud properties in the Equatorial Pacific. *J. Geophys. Res.*, **98,** 18 489–18 500.

Coakley, J. A., and P. Chylek, 1975: The two-stream approximation in radiative transfer: Including the angle of the incident radiation. *J. Atmos. Sci.*, **32,** 409–418.

Driedonks, A. G. M., and P. G. Duynkerke, 1989: Current problems in the stratocumulus-topped atmospheric boundary layer. *Bound.-Layer Meteor.*, **46,** 275–304.

Ecklund, W. L., D. A. Carter, and B. B. Balsley, 1988: A UHF wind profiler for the boundary layer: Brief description and initial results. *J. Atmos. Oceanic. Technol.*, **5,** 432–441.

Fairall, C. W., J. E. Hare, and J. B. Snider, 1990: An eight-month sample of marine stratocumulus cloud fraction, albedo, and integrated liquid water. *J. Climate,* **3,** 847–864.

Feigelson, E. M., 1984: *Radiation in a Cloudy Atmosphere.* D. Reidel Publishing Co., 293 pp.

Feingold, G., B. Stevens, W. R. Cotton, and R. L. Walko, 1994: An explicit cloud microphysics/LES model designed to simulate the Twomey effect. *Atmos. Res.,* **33,** 207–233 .

Frisch, A. S., C. W. Fairall, and J. B. Snider, 1994: Measurement of stratus cloud and drizzle parameters with a $K_u$-band Doppler radar and a microwave radiometer. *J. Atmos. Sci.*, **52,** 2788–2799.

Han, Q., W. B. Rossow, R. Welch, A. B. White, and B. Wielicki, 1994: Validation of cloud microphysics and liquid water path retrievals during FIRE II. *J. Atmos. Sci.,* submitted.

Hignett, P., 1991: Observations of diurnal variation in a cloud-capped marine boundary layer. *J. Atmos. Sci.,* **48,** 1474–1482.

Hogg, D. C., F. O. Guiraud, J. B. Snider, M. T. Decker, and E. R. Westwater, 1983: A steerable dual-channel microwave radiometer for measurement of water vapor and liquid in the atmosphere. *J. Climate Appl. Meteor.,* **22,** 789–806.

Kropfli, R. A., S. Y. Matrosov, T. Uttal, B. W. Orr, A. S. Frisch, K. A. Clark, B. W. Bartram, R. F. Reinking, and J. B. Snider, 1995: Cloud physics studies with 8-mm-wavelength radar. *Atmos. Res.,* **35,** 299–313.

Minnis, P., P. W. Heck, D. R. Young, C. W. Fairall, and J. B. Snider, 1992: Stratocumulus cloud properties derived from simultaneous satellite and island-based instrumentation during FIRE. *J. Appl. Meteor.,* **31,** 317–339.

Pasqualucci, F. B., B. W. Bartram, R. A. Kropfli, and W. R. Moninger, 1983: A millimeter-wavelength dual-polarization Doppler radar for cloud and precipitation studies. *J. Climate Appl. Meteor.,* **22,** 758–765.

Rossow, W. B., and R. A. Schiffer, 1991: ISCCP cloud data products. *Bull. Amer. Meteor. Soc.,* **72,** 2–20.

Schubert, W. H., S. K. Cox, P. E. Ciesielski, and C. M. Johnson-Pasqua, 1987: Operation of a ceilometer during the FIRE marine stratocumulus experiment. Department of Atmospheric Science Paper 420, Colorado State University, Fort Collins, CO, 28 pp.

Stephens, G. L., 1978: Radiation profiles in extended water clouds. II: Parameterization schemes. *J. Atmos. Sci.,* **35,** 2123–2132.

——, S. Ackerman, and E. A. Smith, 1984: A shortwave parameterization revised to improve cloud absorption. *J. Atmos. Sci.,* **41,** 687–690.

Twomey, S., 1977: The influence of pollution on the shortwave albedo of clouds. *J. Atmos. Sci.,* **34,** 1149–1152.

Uttal, T., and J. M. Intrieri, 1993: Comparison of cloud boundaries measured with 8.6-mm radar and 10.6-$\mu$m lidar. Preprints, *Topical Symp. on Combined Optical–Microwave Earth and Atmosphere Sensing,* Albuquerque, NM, Institute of Electrical and Electronics Engineers, 107–110.

VanZandt, T. E., J. L. Green, K. S. Gage, and W. L. Clark, 1978: Vertical profiles of refractivity turbulence structure constant: Comparison of observations by the Sunset Radar with a new theoretical model. *Radio Sci.,* **13,** 819–829.